CONDENSED MATTER

Photo- and Thermoelectric Phenomena in Two-Dimensional Topological Insulators and Semimetals Based on HgTe Quantum Wells (Scientific Summary)

Z. D. Kvon[a, b, *], M. L. Savchenko[a, b], D. A. Kozlov[a, b], E. B. Olshanetsky[a], A. S. Yaroshevich[a], and N. N. Mikhailov[a, b]

[a] Rzhanov Institute of Semiconductor Physics, Siberian Branch, Russian Academy of Sciences, Novosibirsk, 630090 Russia
[b] Novosibirsk State University, Novosibirsk, 630090 Russia
*e-mail: kvon@isp.nsc.ru

Experimental studies of photo- and thermoelectric phenomena in two-dimensional topological insulators and semimetals based on HgTe quantum wells have been briefly reviewed.

1. INTRODUCTION

Since the properties of HgTe quantum wells are completely determined by relativistic effects, these quantum wells have been actively studied during the last 10–15 years because they can be used to implement a number of fundamentally new low-dimension electron systems. For this reason, we begin with a brief analysis of their energy spectrum. Figure 1a shows the qualitative dependence of the energy of the bottom of the main size-quantized subbands in a HgTe quantum well on its thickness d. It is seen that the behavior of the spectrum fundamentally depends on the thickness of the well, and it can be conditionally separated into three regions. In the first region at $d < d_c$, a two-dimensional direct-band-gap insulator is implemented with the band gap decreasing with increasing thickness; this band gap is closed at a critical well thickness of $d_c = 6.2–6.5$ nm depending on the orientation and deformation of the quantum well. With a further increase in d, the second region appears, where a two-dimensional insulator exists with inverted bands (two-dimensional topological insulator) [1–3]. Finally, at $d > 14–16$ nm, a semimetal state appears [4, 5] because of the overlapping of hole-like bands H1 (conduction band) and H2 (valence band). Since we discuss below the properties of two-dimensional (2D) topological insulators (TIs) and 2D semimetals, only the second ($d = 8–9$ nm) and third ($d = 20–22$ nm) regions are of interest. The band structure of 2D TIs calculated in [6] for the (100) and (013) surfaces is shown in Fig. 1b. It is seen that the main characteristics of this band structure slightly depend on the orientation of the surface. In both cases, the critical thick-

ness is $d_c = 6.2–6.3$ nm. It is also seen that the state of the 2D TI with the maximum band gap, which is characterized by the simplest $s–p$ inversion, occurs at a thickness of 8.2–8.5 nm. In this case, the width of the band gap is approximately 30 meV. The dispersion law for edge and bulk states in an 8.5-nm quantum well with the (013) orientation is shown in Fig. 1c. Figure 2 shows the band structure of a two-dimensional semimetal in a 20-nm quantum well with the (100) orientation. The most interesting results of experimental studies of the photo- and thermoelectric properties of the listed systems are briefly described in this work.

2. TERAHERTZ AND MICROWAVE PHOTORESISTANCE OF TWO-DIMENSIONAL TOPOLOGICAL INSULATOR [7, 8]

We first describe experimental samples used to study the photoelectric properties of the two-dimensional topological insulator. They had a special geometry of mesoscopic Hall field-effect transistor and were fabricated from 8–8.3 nm HgTe quantum wells by means of photolithography with the subsequent deposition of an insulator and a semitransparent metal gate. The photograph of a typical sample is shown in Fig. 3a. Figure 3b shows its transport characteristics, namely, the Hall resistance $R_H(V_g^{eff})$ and local resistance $R_{1645}^L(V_g^{eff})$, which was measured in the shortest part of the sample where the distance between potentiometric contacts (contacts 4 and 5 in Fig. 3a) was 2.8 μm, as functions of the effective gate voltage $V_g^{eff} = V_g – V_g^{max}$, where V_g is the gate voltage and V_g^{max}
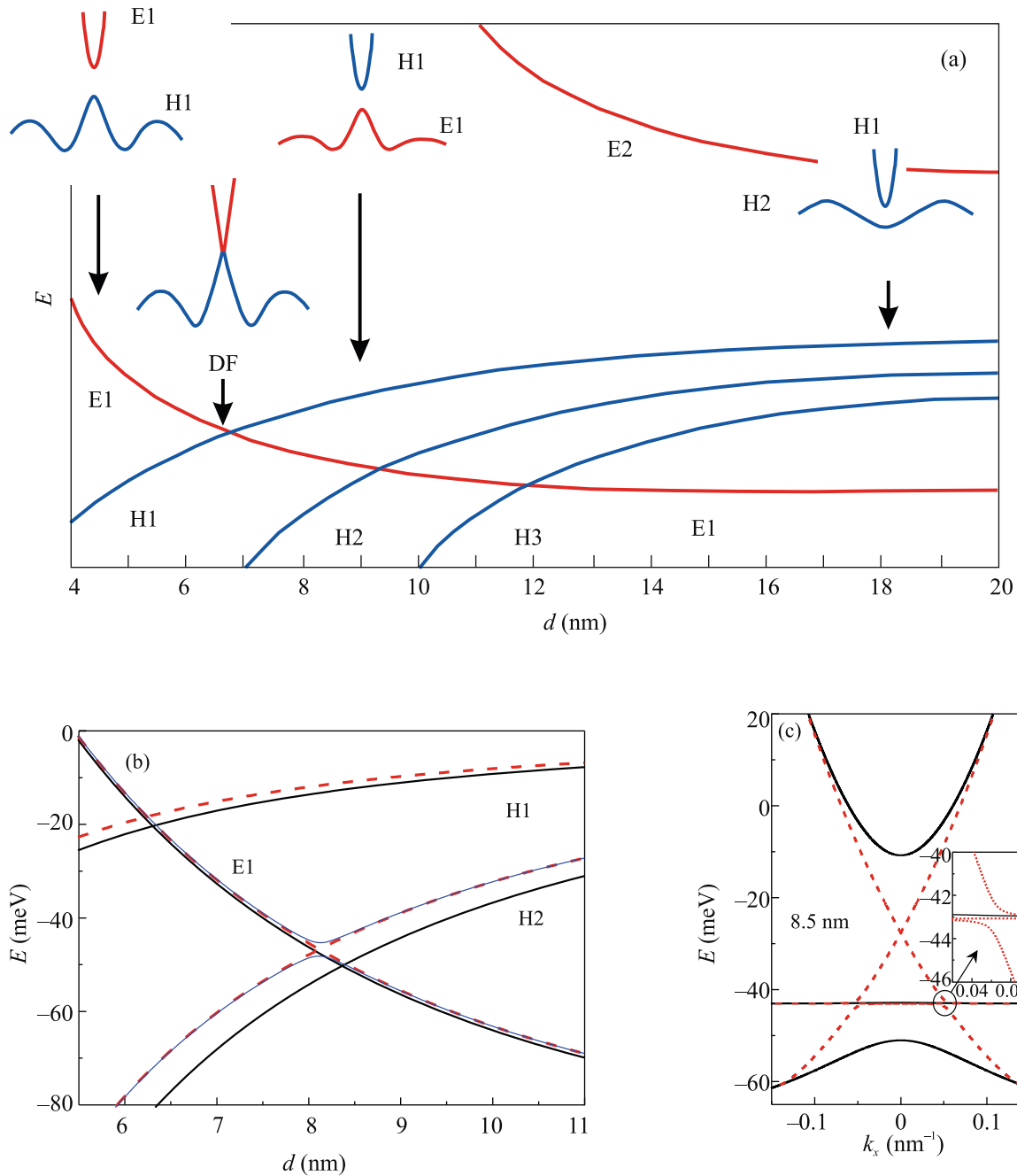
Fig. 1. (Color online) (a) Qualitative behavior of the energy of the bottoms of size-quantized subbands (E1 and E2 are the energies of the bottoms of electron subbands and H1, H2, and H3 are the energies of the bottoms of hole subbands) of the HgTe quantum well versus its thickness. (b) Energy of the bottom of subbands versus the thickness dependence of the quantum well in the range of 5.5−11 nm for the (solid lines) (100) and (dashed lines) (013) surface orientations. (c) Dispersion law of bulk and edge states for the HgTe quantum well with the (013) orientation and thickness $d = 8.5$ nm [6].

is the gate voltage corresponding to the maximum of the local resistance. The observed picture qualitatively coincides with that obtained for all two-dimensional TIs in HgTe quantum wells [1, 2, 9, 10]. The resistance is low (about 1 kΩ/square) at shifts corresponding to the position of the Fermi level (E_F) in the conduction band; passes through a maximum (equals in this case 13.4 kΩ) at the charge neutrality point (CNP), which coincides with V_g^{max} (in this case, E_F passes through the Dirac point); then begins to decrease; and reaches several kiloohms per square when the Fermi level enters the valence band. In this case, the function
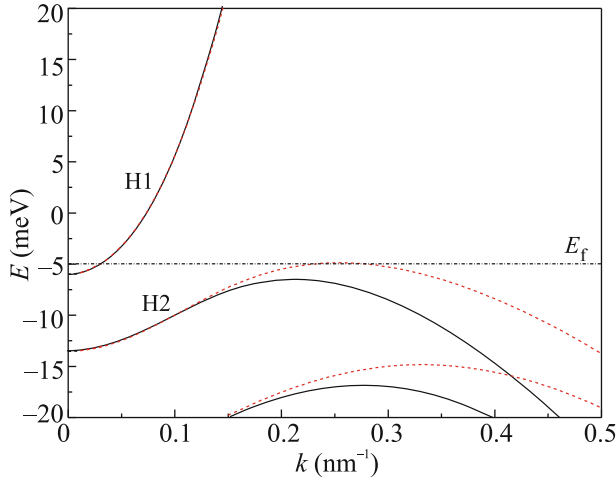
Fig. 2. (Color online) Dispersion law in the conduction and valence bands of the 20-nm-thick HgTe quantum well with the (100) orientation.

$R_H(V_g^{eff})$ becomes zero and change sign. Figure 3c shows the behavior of the nonlocal resistance of the sample $R_{4857}^{nL}(V_g^{eff})$, when contacts 4−8 and 5−7 are used as current and potentiometric contacts, respectively. As expected, the nonlocal resistance signal is much smaller than the local resistance signal when the Fermi level is located in allowed bands. At the same time, the former signal at the CNP is almost three times larger than the local signal, which confirms the edge character of transport. We now analyze the presented data. The local resistance R_{1645}^L at the maximum is close to $h/2e^2$ (which is indicated by the red dotted line in Fig. 3b). This means that an almost ballistic transport occurs in the smallest (about 10 μm along the edge of the sample) segment of the studied Hall structure. The nonlocal resistance R_{4857}^{nL} is determined by the division of the current flowing through contacts 4−8 between a part of the sample with ballistic transport and a part with diffusion transport. Therefore, this resistance lies between $2h/e^2$ and h/e^2. The values $h/(2e^2)$ and h/e^2 are indicated by the red horizontal straight lines in Figs. 3b and 3c, respectively.

Typical results for the measured local photoresistance $\Delta R_{1645}^L(V_g^{eff})$ of the sample irradiated by terahertz 118-μm radiation with a power of about 20 mW as a function of the effective gate voltage are shown in Fig. 4a in comparison with $R_{1645}^L(V_g^{eff})$. The behavior of the nonlocal photoresistance $\Delta R_{4857}^{nL}(V_g^{eff})$ at the same power is shown in Fig. 4b in comparison with $R_{4857}^{nL}(V_g^{eff})$. We now describe the presented data. It is clearly seen that the local and nonlocal photoresis-
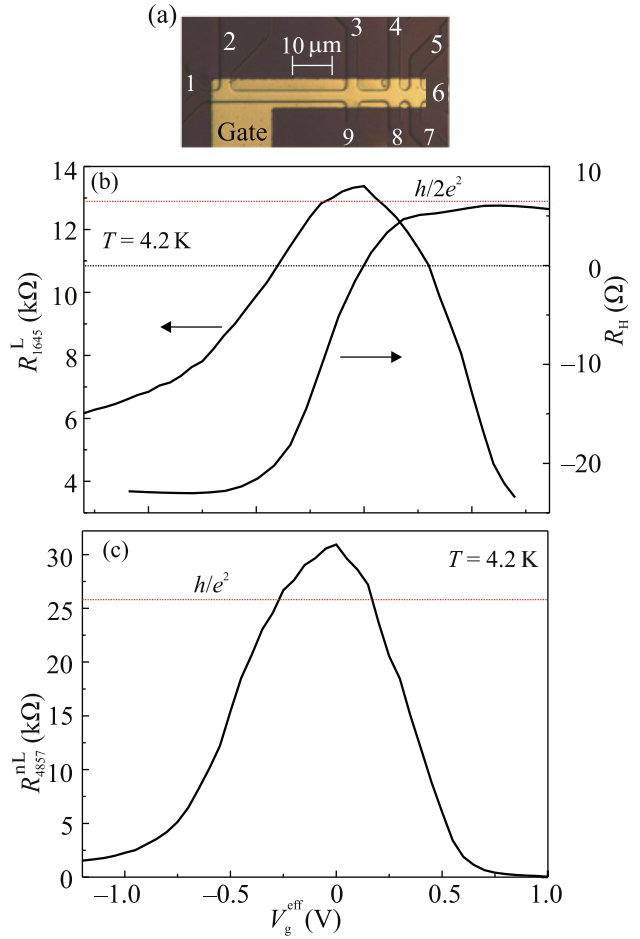

Fig. 3. (Color online) (a) Photograph of the microstructure with a special Hall geometry. (b) Local resistance $R_{1645}^L(V_g^{eff})$ at $B = 0$ and the Hall resistance $R_H(V_g^{eff})$ at $B = 1$ T versus the effective gate voltage. (c) Nonlocal resistance $R_{4857}^{nL}(V_g^{eff})$ versus the effective gate voltage.

tances are almost zero when the Fermi level is located in allowed bands and become nonzero only when the Fermi level enters the band gap; it is remarkable that the photoresistance is negative; i.e., the resistance of the sample decreases under irradiation. At the CNP, both dependences pass through a maximum, where they reach 0.1−0.5% of the total resistance. We now discuss these results. In our case, three types of transitions are possible (inset of Fig. 4b): (i) between Dirac branches of one-dimensional edge states, (ii) between the electron Dirac branch and the conduction band, and (iii) between the valence band and the hole Dirac branch. Transitions of types (ii) and (iii) obviously would give maxima of the photoresistance near allowed bands, i.e., to the right (for the second-type transitions) or to the left (for transitions of the third type) of the CNP on the dependences of the photoresistance on V_g^{eff}. Such a behavior is not observed in the
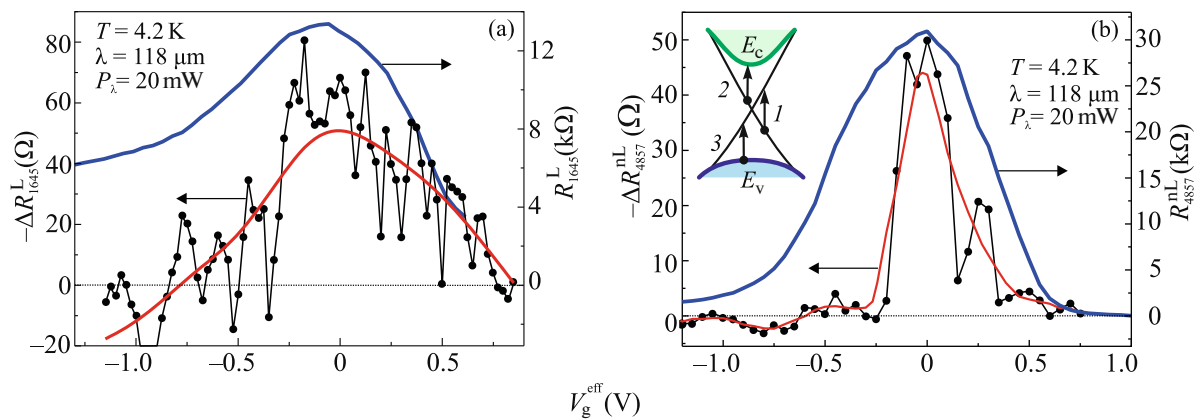
Fig. 4. (Color online) (a) Local resistance and terahertz photoresistance versus the effective gate voltage. (b) Nonlocal resistance and terahertz photoresistance versus the effective gate voltage; the inset shows the possible types of optical transitions under terahertz irradiation.

experiment. Thus, the analysis of the performed measurements of the terahertz photoresistance shows that it is most likely due to optical transitions between edge branches. The previous analysis of absorption on the indicated transitions showed that dipole transitions between edge Dirac branches are forbidden, and only much weaker magnetic dipole transitions occur. However, it was recently found [11] that this conclusion is invalid for HgTe quantum wells because it ignores the violation of space inversion symmetry at the interfaces between these wells and barrier HgCdTe layers. The authors of [11] showed that direct dipole transitions between edge branches are allowed because of the violation of space inversion symmetry at the indicated interfaces and obtained expressions for the absorption coefficient. Thus, the experimental conclusion that the observed terahertz photoresistance of the 2D TI in the HgTe quantum well is caused by transitions between edge branches was confirmed theoretically in [11]. The photoresistance caused by a similar mechanism was also detected in the microwave response of a sample to irradiation in the frequency range of 110–169 GHz (Fig. 5). The study of the microwave photoresistance in samples with a small bulk leakage (the bulk resistance is only an order of magnitude higher than the edge resistance) revealed an additional mechanism associated with the action of radiation on the bulk (Fig. 6), which is observed only in the nonlocal geometry. It can be explained as follows. Radiation incident on the sample changes the bulk resistance by means of the heating effect. Thus, it changes the magnitude of bulk leakage, but this change is so small that its contribution is not observed in local-geometry measurements because it is added to a much lower resistance of the edge channel. The response of the nonlocal resistance to change in the bulk conductivity should be much stronger. In the local geometry, $\Delta R^{\mathrm{L}} \approx \Delta \rho_{xx}(R_{\mathrm{edge}}/\rho_{xx})^2$, where R_{edge} is the edge resistance. In the nonlocal geometry,
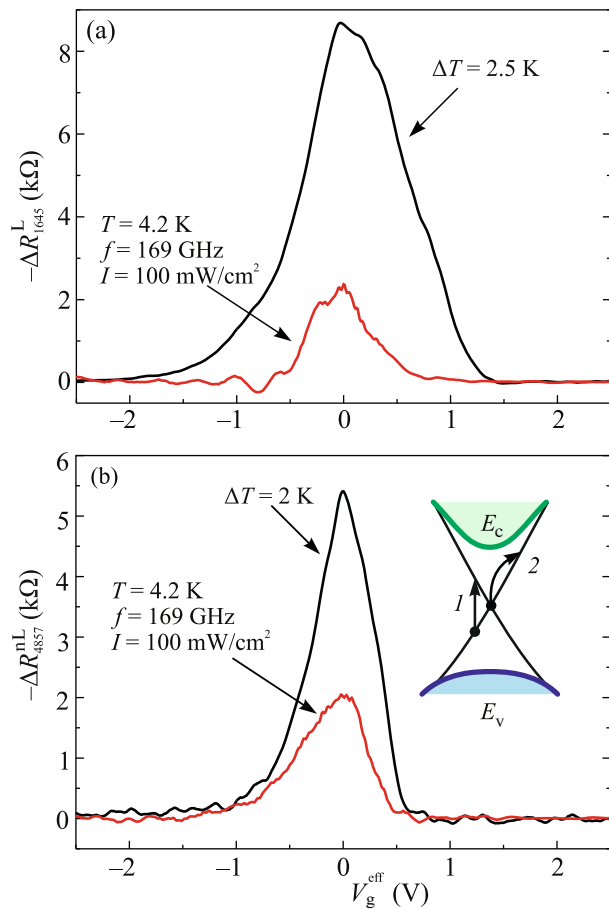
Fig. 5. (Color online) (a) Local microwave photoresistance $\Delta R^{\mathrm{L}}_{1645}(V_g^{\mathrm{eff}})$ and the heat-induced addition $\Delta R^{\Delta T}(V_g^{\mathrm{eff}})$ versus the effective gate voltage. (b) Nonlocal microwave photoresistance $\Delta R^{\mathrm{nL}}_{4875}(V_g^{\mathrm{eff}})$ and the heat-induced addition $\Delta R^{\Delta T}(V_g^{\mathrm{eff}})$ versus the effective gate voltage.
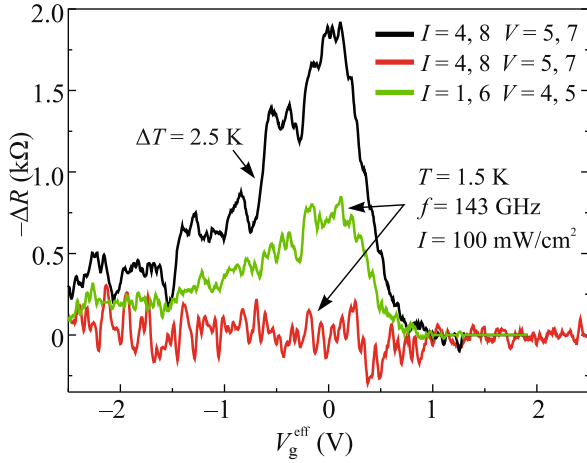
**Fig. 6.** (Color online) Local $\Delta R^{L}_{1645}(V^{eff}_{g})$ and nonlocal $\Delta R^{nL}_{4857}(V^{eff}_{g})$ microwave photoresistance, as well as the heat-induced addition $\Delta R^{\Delta T}(V^{eff}_{g})$, versus the effective gate voltage for samples with bulk leakage.

$\Delta R^{nL} \approx \Delta\rho_{xx} \exp(-\pi L/W)$, which is an order of magnitude larger than ΔR^{L}.

3. PHOTOGALVANIC EFFECT IN THE TWO-DIMENSIONAL TOPOLOGICAL INSULATOR [12]

The schematic diagram of the experiment for the observation of the photogalvanic effect performed with the described samples is shown in Fig. 7. The sample was irradiated by circularly polarized terahertz radiation at wavelengths of 118 and 184 μm. As seen in Fig. 1c, the energies of photons (10.4 and 6.7 meV) at both wavelengths are smaller than the width of the bulk gap by a factor of 3−5. Then, as mentioned in Section 2, three types of optical transitions are possible under irradiation (see Fig. 4b): (i) transitions between edges branches, (ii) transitions from the edge branch to the conduction band, and (iii) transitions from the valence band to the edge branch. According to theories of the photogalvanic effect in 2D TIs developed in [12−14], all three types of transitions can lead to the appearance of a chiral spin photocurrent along the perimeter of the sample in the direction determined by the sign of the circular polarization, as shown in Fig. 7a. The key experimental result is presented in Fig. 7b, which shows the dependence of the photocurrent generated by terahertz radiation at a wavelength of 118 μm on the gate voltage as measured between two opposite pairs of contacts 4−3 and 8−9. This figure clearly demonstrates that change in a pair of contacts leads to change in the sign of the photocurrent, as expected in the case of its flow along the perimeter of the experimental sample. Figure 7c demonstrates another experimental result of change in
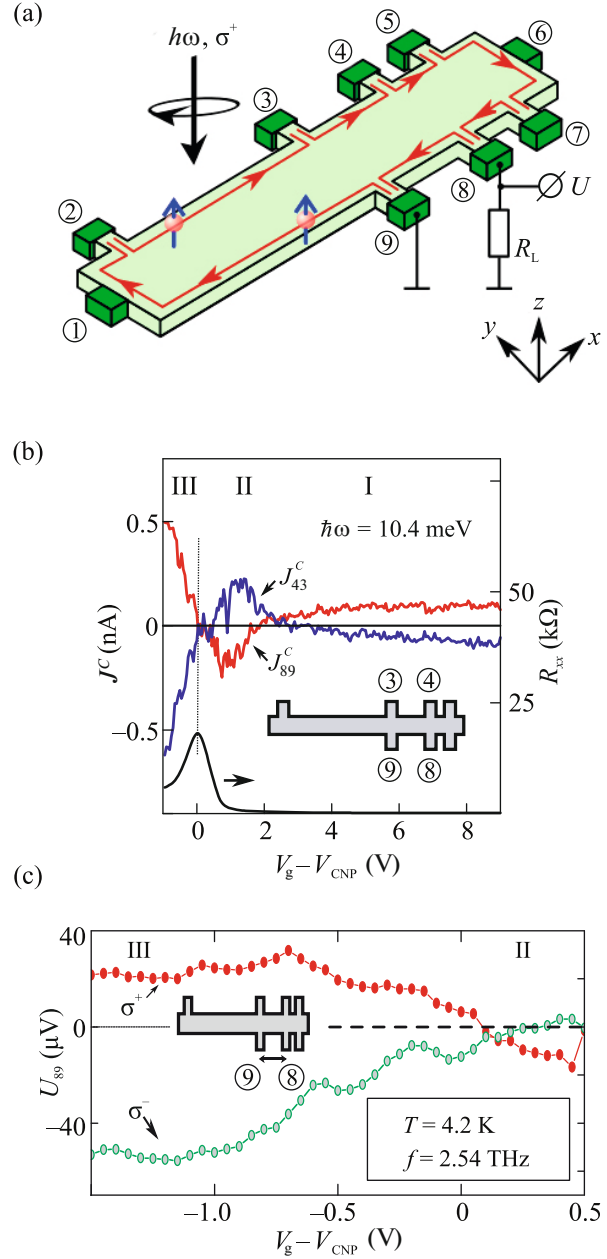
Fig. 7. (Color online) (a) Geometry of the experiment for the observation of the circular photogalvanic effect in the two-dimensional topological insulator. (b) Edge photocurrent measured through contacts 4−3 and 8−9: the Fermi level is (I) in the conduction band, (II) between the CNP and the bottom of the conduction band, and (III) between the CNP and the top of the valence band. (c) Photovoltage measured on contacts 8−9 for two signs of the circular polarization of 2.54-THz radiation incident on the sample.

the sign of the photocurrent at change in the sign of the circular polarization. We now analyze the data shown in Figs. 7b and 7c, beginning with the dependence of the photocurrent on the gate voltage shown in Fig. 7b in the widest gate voltage range. The lower part
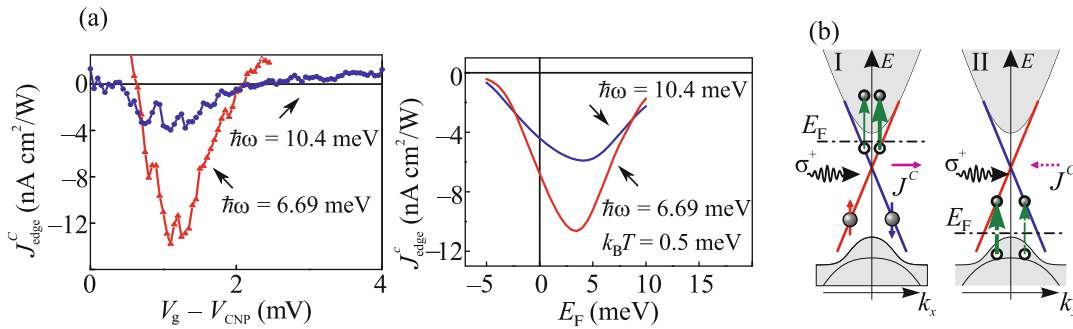
Fig. 8. (Color online) (a) (Left part) Experimental edge photocurrent versus the gate voltage for frequencies of 1.2 and 2.54 THz and (right part) the calculated edge photocurrent versus the Fermi energy for the same frequencies. (b) Optical transitions between (I) edge states and the conduction band and (II) the valence band and edge states under circularly polarized irradiation.

of this figure shows the dependence of the resistance of the studied sample on the gate voltage. The position of its maximum V_g^{max} makes it possible to determine the charge neutrality point ($V_{CNP} = V_g^{max}$) and thereby to analyze the behavior of the photocurrent at all fundamentally important positions of the Fermi level. When the Fermi level is in the conduction band, a low photocurrent is observed and decreases as E_F approaches the bottom of the conduction band. Further, when E_F enters the band gap, the photocurrent changes sign and its magnitude begins to increase as the Fermi level is shifted inside the band gap. Then, this increase ceases and the photocurrent passes through the maximum, which corresponds to the position of the Fermi level between the middle of the band gap and the bottom of the conduction band. When the Fermi level approaches the CNP, the photocurrent decreases rapidly, changes sign at the CNP, and then begins to increase strongly as E_F approaches the valence band. The comparison of the experimental behavior of the photocurrent described above with the mentioned theories of the photogalvanic effect [12, 14] shows that this behavior is most adequately described by transitions between edge states and the conduction band. This is illustrated in Fig. 8a, which demonstrates satisfactory agreement between theories and experiments when the Fermi level is between the middle of the band gap and the bottom of the conduction band. According to these theories, the photogalvanic effect occurs because the probabilities of transitions between edge states and the conduction band (excited by circularly polarized radiation) are different for branches with different spin directions (for illustration, see Fig. 8b). The proposed theories do not explain the change in the sign of the photocurrent at the CNP. Such discrepancy with experiment occurs most likely because the developed theories [12, 14] ignore a complex structure of the valence band of HgTe quantum wells, which is due to the strong effect of lower lying states on the formation of wavefunctions near the top of the main valence subband. Finally, we

note that the simplest and most efficient model of the photogalvanic effect proposed in [13] has not yet been implemented in experiments. This was previously explained by the fact that only weak direct magnetic dipole transitions between edge branches are allowed (*I* in the inset of Fig. 4b). However, the authors of [11] recently showed that direct dipole transitions observed in the microwave and terahertz photoresistances are allowed because of the violation of space inversion symmetry at the HgTe/CdHgTe interface. The detection of the photogalvanic effect associated with these transitions requires more detailed experiments.

4. CYCLOTRON RESONANCE PHOTOCONDUCTIVITY IN A HIGHLY IMBALANCED TWO-DIMENSIONAL SEMIMETAL [15]

One of the features of a two-dimensional semimetal existing in HgTe quantum wells [4] is the possibility of using it to obtain a state with different relations between the electron (n_s) and hole (p_s) densities [5]. In particular, the transport response of electrons in 20-nm-thick quantum wells with the (100) orientation and the energy spectrum shown in Fig. 2 was observed when the electron density was two orders of magnitude lower than the hole density [16]. The mentioned property of this system allows studying two-dimensional electrons in a quite specific situation where they do not move among similar quasiparticles but are immersed in a hole liquid, which screens the impurity fluctuation potential. As a result, the motion of electrons at their density of about 10^9 cm^{-2} remains free unlike single-component systems, where a transition to the percolation regime occurs at such densities even in the purest AlGaAs/GaAs systems [17]. The cyclotron resonance photoconductivity of such an electron gas was studied in macroscopic Hall field-effect bars with a semitransparent gate. The photograph of such a bar with indicated sizes is shown in Fig. 9a. Figure 9b shows typical magnetic field dependences of the pho-
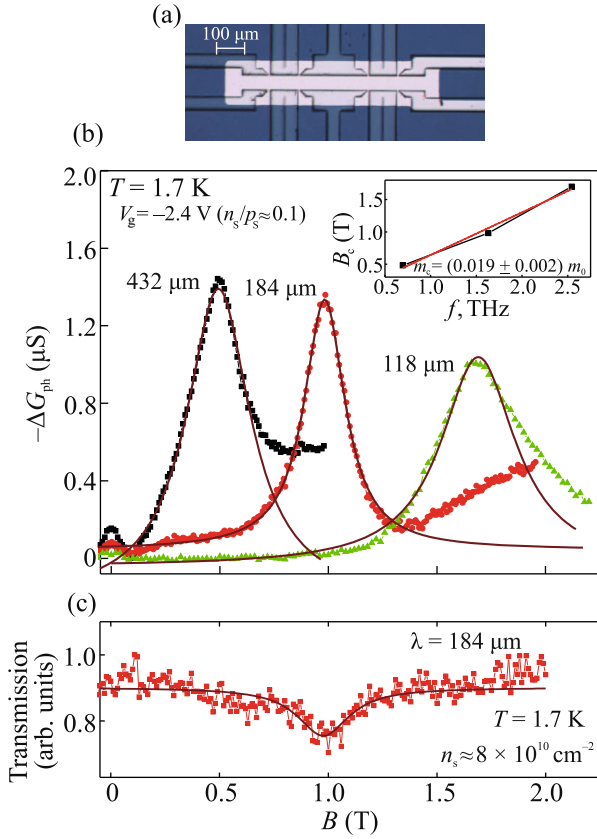
Fig. 9. (Color online) (a) Photograph of the Hall structure with the semitransparent gate. (b) Magnetic-field dependence of the photoconductivity $\Delta G_{ph}(B)$ at the wavelengths of the incident radiation $\lambda = 432$, 184, and 118 μm for the gate voltage $V_g = -2.5$ V ($n_s/p_s \approx 0.1$). The inset shows the frequency dependence of the position of the cyclotron resonance. (c) Magnetic-field dependence of the transmission signal for the entire sample at $\lambda = 184$ μm and $n_s \approx 8 \times 10^{10}$ cm^{-2} (see main text). The solid lines are the Lorentzian approximations.

toconductivity ΔG_{ph} in a sample irradiated by terahertz radiation at wavelengths of 432, 184, and 118 μm. The resonance behavior of the photoconductivity with peaks at magnetic fields $B_c = 0.5$, 1, and 1.7 T for wavelengths of 432, 184, and 118 μm, respectively, is clearly seen. Figure 9c shows the magnetic field dependence of the transmission signal of the entire sample with an electron density of 8×10^{10} cm^{-2} at $\lambda = 184$ μm. It is noteworthy that the position of resonance makes it possible to determine the effective cyclotron mass, which was found to be $m_c = (0.019 \pm 0.002)m_0$.

The main result of the work is presented in Fig. 10, which shows the magnetic field dependences of the photoconductivity for $\lambda = $ (a) 432 and (b) 118 μm at several gate voltages corresponding to the condition $n_s/p_s < 0.2$. It is remarkable that resonance is observed

even at $V_g = -9.7$ V, when $n_s/p_s \sim 10^{-3}$ and the magnetotransport response demonstrates no signatures of the existence of electrons. The electron density is so low that cyclotron resonance for all wavelengths corresponds to the transition from the partially filled zeroth Landau level (with the filling factor in the range $1 \geq \nu \geq 0.08$) to the first level. Since this transition occurs between two discrete levels, it is reasonable to assume that the shape of the photoconductivity signal should be phenomenologically described by Lorentzian dependences. These dependences are shown by solid lines in Fig. 10 and, as seen, describe the experiment well. The inset of Fig. 10b shows the dependences of the width γ_c of the resonance in units of B_c on the electron density for 432 and 118 μm. The width γ_c is in the range of $0.3-0.8$ and slightly depends on the electron density. This width corresponds to the energy broadening of the resonance by $1-3$ meV. It is interesting to compare it to the transport broadening of the Landau level, using the following well-known expression for it in the case of a short-range potential [18]:

$$\Gamma^2 = (2/\pi)\hbar\omega_c(\hbar/\tau_{tr}), \qquad (1)$$

where $\tau_{tr} = (m_n/e)\mu_n$, ω_c is the cyclotron frequency, and μ_n is the electron mobility. According to Eq. (1) with the mobility $\mu_n = 2 \times 10^5$ cm^2/(V s) corresponding to our case, $\Gamma \approx 0.8-1.2$ meV, which corresponds to experimental values. Thus, the photoconductivity measured in the reported experiment is well described as the cyclotron resonance photoconductivity caused by transitions between Landau levels, which are broadened because of the short-range scattering potential. We now analyze the density dependence of the amplitude of the photoconductivity. As seen in Fig. 10, the photoconductivity signal does not vanish when the electron density decreases from 2×10^{10} to 10^9 cm^{-2}. When the electron density decreases by more than an order of magnitude, the amplitude of the photoconductivity at $\lambda = 118$ μm is only halved. At the wavelength of incident radiation $\lambda = 432$ μm, the amplitude of the photoconductivity first increases with a decrease in the electron density to $n_s/p_s \approx 0.01$ and then decreases to the initial values at $n_s/p_s \approx 0.1$. Thus, the amplitude of the photoconductivity is approximately the same at $n_s/p_s \approx 0.1$ and 0.001; i.e., it remains almost the same at a decrease in the electron density by two orders of magnitude. The described behavior of the photoconductivity means that the formation of the cyclotron resonance photoconductivity cannot be explained by a simple mechanism when it is proportional to the intensity of radiation absorption because the absorption coefficient should be proportional to the density of electrons at the zeroth Landau level. It is necessary to significantly enhance the effective electric field of incident tera-
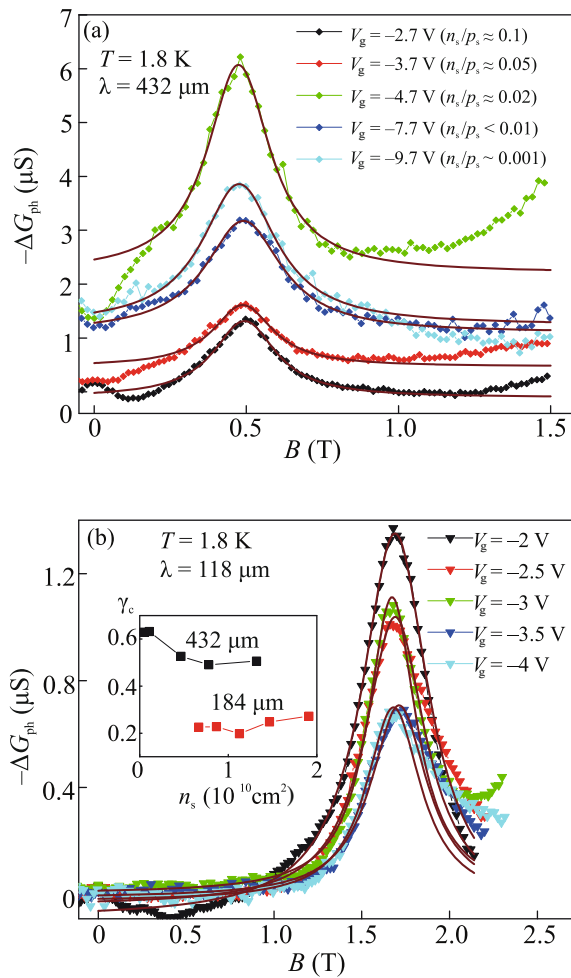
Fig. 10. (Color online) Photoconductivity $\Delta G_{ph}(B)$ for (a) 432 and (b) 118 μm at several gate voltages corresponding to the condition $n_s/p_s \lesssim 0.1$. The inset shows the concentration dependence of the width γ_c of resonance photoconductivity peaks divided by B_c, as determined from the Lorentizian approximation of lines.

hertz radiation acting on an electron. Recently, the authors of [19] developed a theory according to which a strong enhancement of the electric field of radiation acting on the electron can be due to its interaction with other electrons. Magnetoplasma effects are also not excluded [20]. However, a more certain solution to the formulated problem requires both further experiments and the development of a theory closest to the considered situation.

5. THERMOPOWER OF A TWO-DIMENSIONAL TOPOLOGICAL INSULATOR [21]

In this section, we describe experimental studies of the thermopower of a two-dimensional topological insulator in HgTe quantum wells with an inverted spectrum. The samples were the same mesoscopic Hall field-effect transistors used to study the photoelectric properties of 2D TIs (see Fig. 3a). The scheme of measuring the thermopower is shown in Fig. 11a. A heater in the form of a thin metallic strip with a resistance of ≈ 100 Ω was placed on one side of the sample against one of the current contacts. Through an indium layer deposited on the opposite end of the sample, the sample was in thermal contact with a 5-mm^3 copper thermal anchor, which in turn made contact with a massive copper holder of the sample. To produce the temperature gradient along the sample, an alternating current at a frequency of 0.4–1 Hz with an amplitude up to 60 mA was passed through the metallic strip heater. In the indicated current range, the heater operated in a linear regime. To control the temperature gradient along the sample, we used two calibrated thermistors placed on the sides of the heater and thermal anchor. The temperature difference between contacts 2 and 3 spaced from each other at the largest distance of 35 μm at $T = 4.2$ K and a current of 50 mA through the heater is estimated as $\Delta T \approx 0.02$ K. The thermal conductivity of liquid helium in the working temperature range $T = 2.2–4.2$ K is negligibly low compared to the phonon thermal conductivity of the substrate. Under these conditions, the thermal conductivity of the substrate determined the temperature gradient along the sample. The thermopower signal was measured at the doubled frequency with the use of all potentiometric contacts. We studied about ten samples. The main results are presented in Figs. 11b–11d. Figure 11b shows the dependences of the resistances of all three parts of the sample: between contacts 4 and 5, where ballistic transport occurs; between contacts 3 and 4 with quasiballistic transport; and between the most spaced contacts 2 and 3, where the diffusion charge transport occurs. The measurements of the thermopower from the indicated contacts are presented in Fig. 11c in the form of the dependence of the Seebeck coefficient S on $V_g - V_{CNP}$. It is clearly seen that this dependence is qualitatively the same for all parts of the sample: the thermopower is small when the Fermi level is in the conduction band, increases as the Fermi level moves inside the band gap, then passes through a maximum, and begins to decrease as the Fermi level approaches the CNP. The thermopower changes sign at the CNP and further increases noticeably to the maximum absolute values several times larger than those observed in the upper half of the band gap. Figure 11d demonstrates the dependence of the thermopower and resistance near the maximum of the thermopower to the left of the CNP on the distance between potentiometric contacts. It is seen that the Seebeck coefficient S, unlike R, does not increase with the distance between contacts but has a complex behavior. Such a behavior indicates that the formation of the thermopower in a real topological insulator is not described by a linear law, but strongly depends not only on the state of edge channels but also on the state
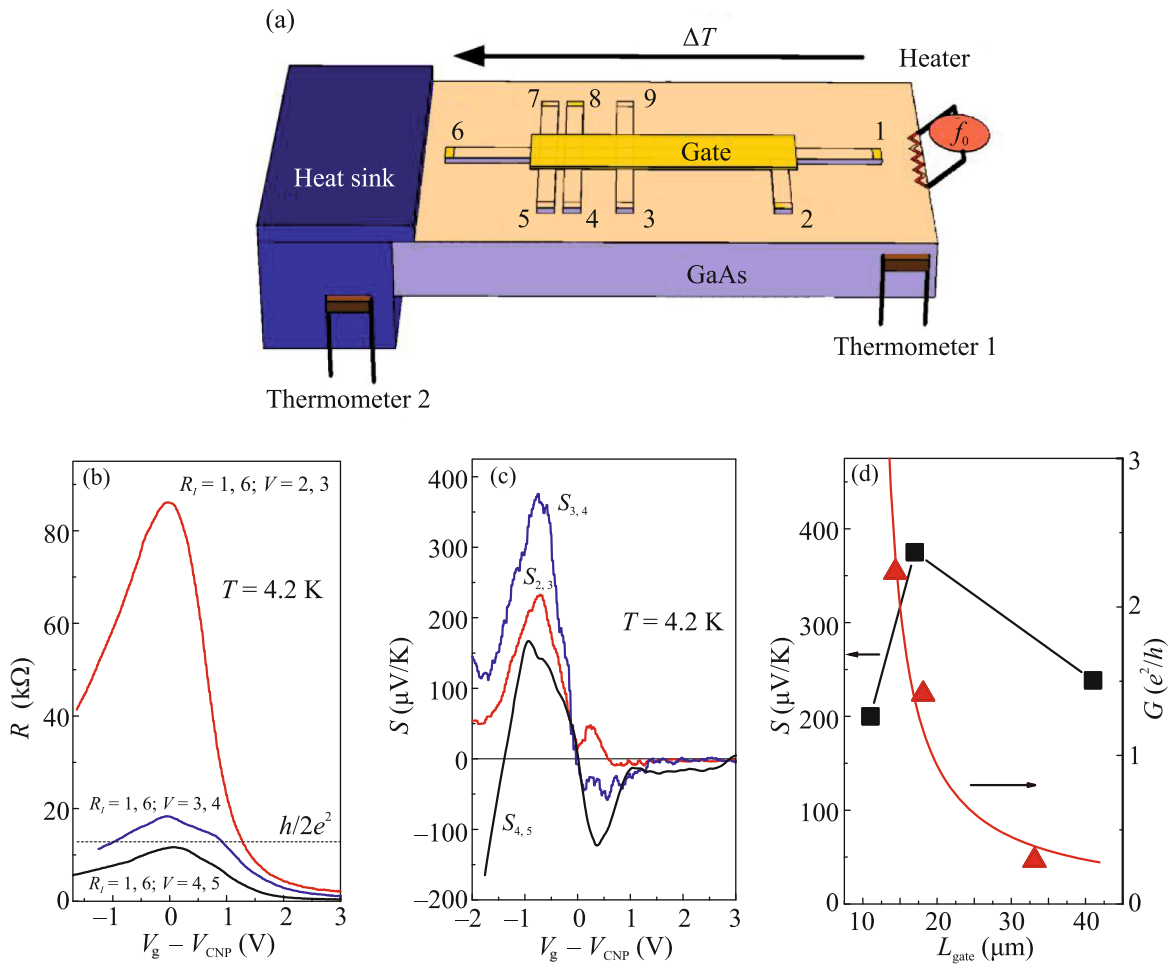
Fig. 11. (Color online) (a) Schematic of the setup for measuring the thermopower of the 2D TI. (b) Resistance of Hall bars with different lengths versus the gate voltage. (c) Seebeck coefficient versus the gate voltage. (d) Conductance and the Seebeck coefficient versus the distance between the potentiometric contacts.

of the bulk and on the character of the interaction between them. The measurement of the temperature dependence shows that the observed thermopower decreases almost linearly with decreasing temperature. A sharp asymmetry of the thermopower signal indicates that this signal is not due to edge channels. Consequently, it remains to assume that the thermopower is mainly due to the bulk contribution. We consider this important statement in more detail. If the total conductivity G_{tot} of the 2D TI is determined by the sum of the edge, G_e, and bulk, G_b, contributions, the measured Seebeck coefficient is given by the formula

$$S_{tot} = (S_e G_e + S_b G_b)/(G_e + G_b). \qquad (2)$$

When the Fermi level is located in the band gap, it is obvious that $G_e \gg G_b$ and Eq. (2) is simplified to the form $S_{tot} = S_e + S_b(G_b/G_e)$. This means that the bulk contribution to the total thermopower is determined not only by S_b but also by the ratio $G_b/G_e \ll 1$. The

calculation of both contributions shows that the bulk contribution can nevertheless dominate. This occurs because S_b in the hopping conductivity regime characteristic of the bulk can be very large because of the strong energy dependence of the density of states. Figure 12 shows (a) the qualitative behavior of the density of states in the HgTe quantum well with the inverted spectrum and (b) the measured Seebeck coefficient in comparison with that calculated within the theory [22], where it is determined as the thermopower associated with hopping conductivity [23] in the bulk band gap of the quantum well. Good agreement is seen. Discrepancy between the experimental and calculated Seebeck coefficients S in the lower part of the band gap can be due to a more complex structure of the tails of the valence band in the real sample than that assumed in the calculation. Thus, the described results indicate that the thermopower of the real two-dimensional TIs in the HgTe quantum well is generated by the bulk of the quantum well in the hopping conductivity regime rather than by edge states, whose role is
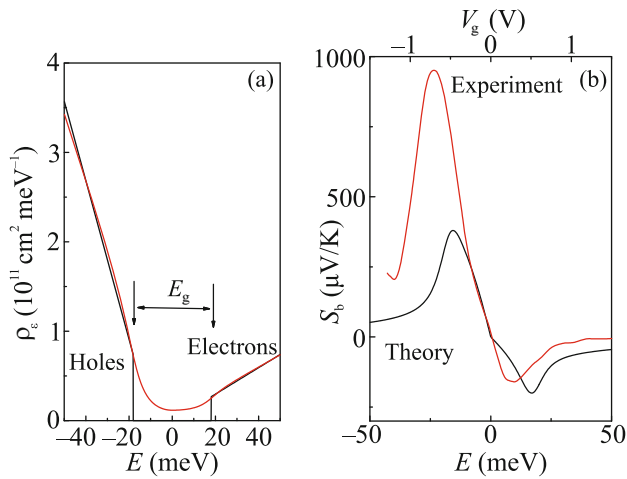
Fig. 12. (Color online) (a) Qualitative behavior of the density of states in the two-dimensional topological insulator in the presence of disorder versus the energy. (b) Energy dependences of experimental and calculated Seebeck coefficients.

reduced to the shunting of the thermopower in view of a much higher conductivity.

6. THERMOPOWER IN THE TWO-DIMENSIONAL SEMIMETAL [22]

The thermopower in the two-dimensional semimetal was studied with a macroscopic Hall field-effect transistor based on a 20-nm-thick quantum well with the (013) orientation, having two bars with the sizes $L \times W = 100 \times 50 \, \mu m$ and $L \times W = 250 \times 50 \, \mu m$. The method of measurement was described in the preceding section. Figure 13a shows the dependences of the resistance on the gate voltage at various temperatures. It is seen that these dependences correspond to the behavior that should be observed in 20-nm HgTe quantum wells, where the (two-dimensional metal–two-dimensional semimetal) transition occurs upon the variation of the gate voltage [5]. The temperature dependence of the resistance changes abruptly at this transition. This dependence is very weak before the transition and is typical of a two-dimensional metal at $k_F l \gg 1$ (k_F is the wavenumber of the electron and l is the mean free path of the electron) and low temperatures, when phonon scattering is almost absent and the temperature dependence is determined by effects of weak localization. After the transition to the semimetal state, the resistance increases noticeably with the temperature because of the electron–hole scattering; consequently, this increase is proportional to the square of the temperature (Fig. 13b). The measured thermopower between potentiometric contacts of the bar with the length $L = 100 \, \mu m$ is shown in Fig. 14 in the form of the dependence of the Seebeck coefficient
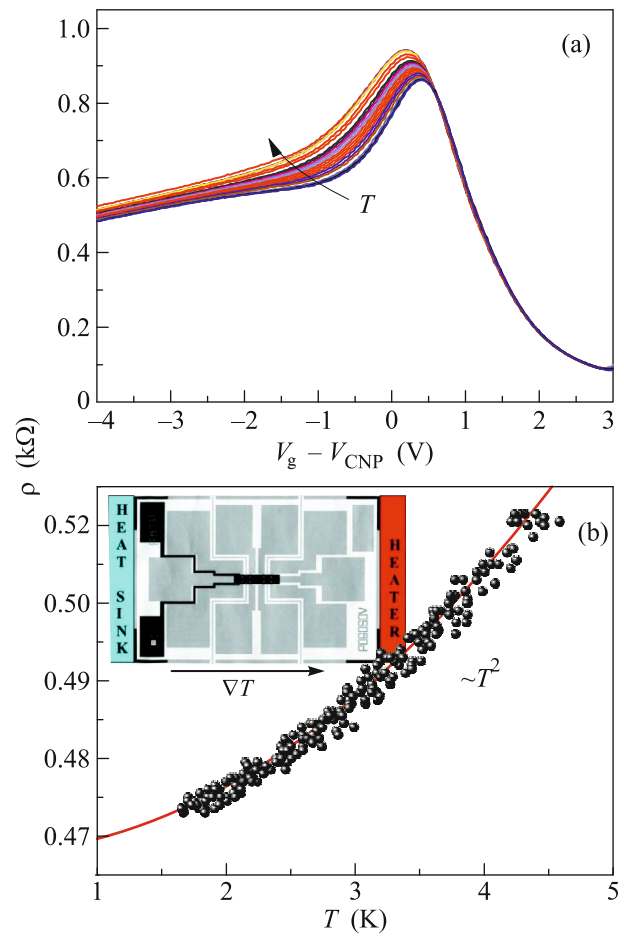

Fig. 13. (Color online) (a) Resistivity of the experimental two-dimensional semimetal sample versus the gate voltage at several temperatures in the range of 2.1–6 K. (b) Temperature dependence of the resistance in the semimetal state $V_g = -5$ V. The inset shows the schematic of the arrangement of the sample when measuring the thermopower.

on the gate voltage at several temperatures. As seen, the Seebeck coefficient S at gate voltages corresponding to the electron metal is relatively small and decreases with increasing density according to the Mott formula for the thermopower in metals. The Seebeck coefficient S changes sign near the CNP and begins to increase linearly in the semimetal state with an increase in the hole density and a decrease in the electron density; the magnitude of the Seebeck coefficient is almost an order of magnitude larger than that observed to the right of the CNP. Plots in Fig. 14 also clearly indicate that the thermopower increases with the temperature in the entire gate voltage range. Magarill and Entin developed a theory of the diffusion thermopower for an electron–hole system [22]. This theory was used to calculate the Seebeck coefficient S in the semimetal state, i.e., to the left of the CNP. For the metal state, i.e., to the right of the CNP, we used
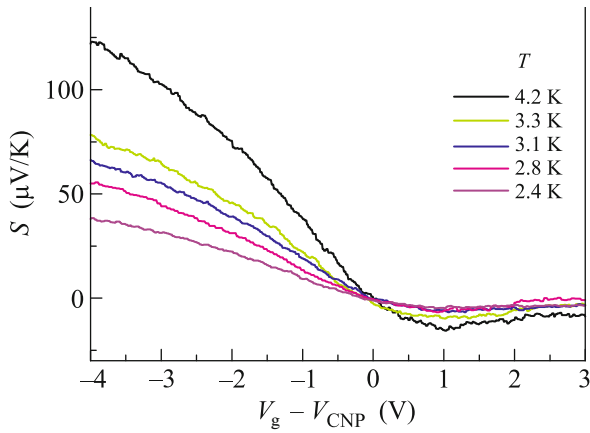
Fig. 14. (Color online) Measured Seebeck coefficient versus the gate voltage at various temperatures.

Fig. 15. (Color online) (a) Experimental and calculated Seebeck coefficients versus the gate voltage. (b) Temperature dependences of the experimental and calculated Seebeck coefficients.

the standard Mott formula [24]. Good agreement between the calculation and experiment for this state is seen (Fig. 15a). On the contrary, agreement between experiment and theory is significantly worse to the left of the CNP in Fig. 15a. In this gate voltage range, the theory underestimates the experimental Seebeck coefficient by a factor of about 4. The observed discrepancy occurs likely because the calculation describes only the diffusion contribution to the thermopower in the semimetal. However, the measured thermopower includes not only the diffusion contribution but also the phonon drag contribution [25], which is ignored in the theory. As known, the magnitude of the phonon drag is proportional to the square of the mass of charge carriers. The masses of electrons and holes in the 20-nm HgTe quantum well are $m_e = 0.025 m_0$ and $m_h = 0.15 m_0$, respectively. For this reason, the contribution of phonon drag is significant to the left of the CNP (i.e., in the region, where holes dominate), whereas it is hardly noticeable to the right of the CNP, where the two-dimensional metal occurs. The points in Fig. 15b are experimental values of the Seebeck coefficient at $V_g = -5$ V as a function of the temperature. It is seen that these values are much larger than the corresponding calculated diffusion contribution. It can be assumed that the difference between the shown experimental and calculated dependences is the contribution to the Seebeck coefficient from the phonon drag in the two-dimensional semimetal when holes dominate. As an example of the phonon drag in a normal two-dimensional metal, we consider the contribution proportional to T^3 [25]. The sum of the diffusion contribution and function $S = A \times T^3$ ($A = 1.6$ μV/K^4) is plotted as the green line through the experimental points in Fig. 15b. It is seen that this line describes well the experimental points in the range of 2.5–3.5 K, but a discrepancy is observed at higher temperatures, where the experimental points are
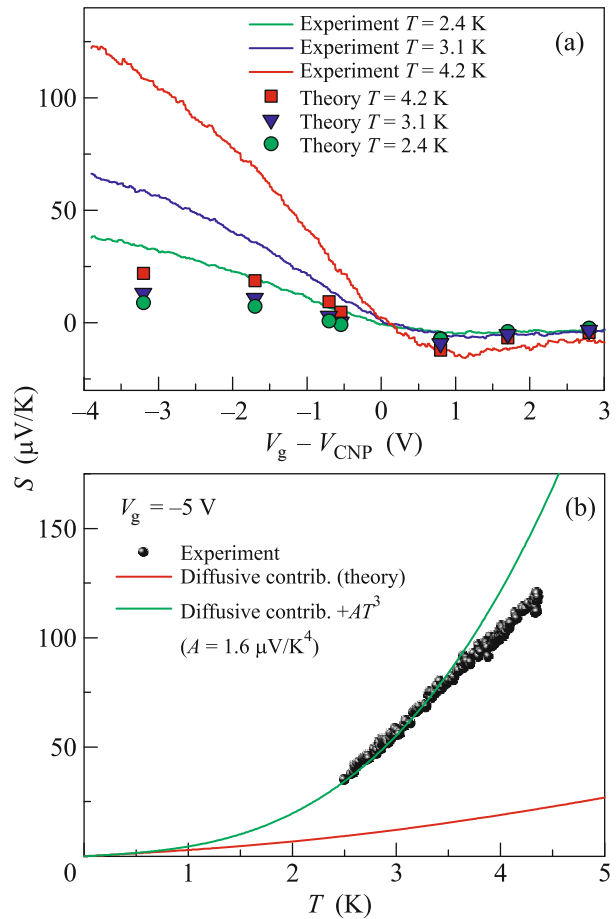
below the calculated line. The observed discrepancy can assumingly be attributed to the temperature-induced enhancement of phonon-dragged holes on electrons, which reduces the measured Seebeck coefficient. However, for a more certain conclusion, it is necessary to develop a theory of the phonon drag in the two-dimensional semimetal in the presence of the electron–hole scattering.

7. CONCLUSIONS

The study of photo- and thermoelectric phenomena in two-dimensional topological insulators and semimetals based on HgTe quantum wells has revealed a number of new interesting effects caused by features of their energy spectrum and processes of scattering in them. This review does not end the described studies but indicates that their continuation in new experiments and further development of the theory is interesting and urgent. In particular, it is of current interest to seek and study the photogalvanic effect in a two-dimensional topological insulator, which is caused by

direct transitions between Dirac branches and was recently predicted in [11], and polarization dependences of the terahertz photoconductivity calculated in [11]. It is also necessary to continue the experimental and theoretical search for the explanation of the anomalous cyclotron resonance photoconductivity in a highly imbalanced two-dimensional semimetal. In the context of thermoelectric effects, the search for the thermopower of the two-dimensional topological insulator caused by edge states is the most intriguing but difficult goal. A consistent detailed study of effects of the phonon drag and Nernst−Ettingshausen effect in two-dimensional semimetals is necessary.

FUNDING

REFERENCES

1. M. Konig, S. Wiedmann, C. Brune, A. Roth, H. Buhmann, L. W. Molenkamp, X.-L. Qi, and S.-C. Zhang, Science (Washington, DC, U.S.) **318** (5857), 766 (2007).

2. M. Konig, H. Buhman, L. M. Molencamp, T. Hughes, C.-X. Liu, X.-L. Qi, and S.-C. Zhang, J. Phys. Soc. Jpn. **77**, 031007 (2008).

3. A. Roth, C. Brune, H. Buhmann, L. W. Molenkamp, J. Maciejko, X.-L. Qi, and S.-C. Zhang, Science (Washington, DC, U. S.) **325**, 294 (2009).

4. Z. D. Kvon, E. B. Olshanetsky, D. A. Kozlov, N. N. Mikhailov, and S. A. Dvoretskii, JETP Lett. **87**, 502 (2008).

5. E. B. Olshanetsky, Z. D. Kvon, M. V. Entin, L. I. Magarill, N. N. Mikhailov, and S. A. Dvoretskii, JETP Lett. **89**, 290 (2009).

6. O. E. Raichev, Phys. Rev. B **85**, 045310 (2012).

7. Z. D. Kvon, K.-M. Dantscher, M.-T. Scherr, A. S. Yaroshevich, and N. N. Mikhailov, JETP Lett. **104**, 716 (2016).

8. A. S. Yaroshevich, Z. D. Kvon, G. M. Gusev, N. N. Mikhailov, JETP Lett. **111**, 121 (2020).

9. G. M. Gusev, Z. D. Kvon, and O. A. Shegai, Phys. Rev. B **84**, 121302(R) (2011).

10. E. B. Olshanetsky, Z. D. Kvon, G. M. Gusev, A. D. Levin, O. E. Raichev, N. N. Mikhailov, and S. A. Dvoretsky, Phys. Rev. Lett. **114**, 126802 (2015).

11. M. V. Durnev and S. A. Tarasenko, J. Phys.: Condens. Matter **31**, 035301 (2019).

12. K.-M. Dantscher, D. A. Kozlov, M. T. Scherr, S. Gebert, J. Barenfänger, M. V. Durnev, S. A. Tarasenko, V. V. Belkov, N. N. Mikhailov, S. A. Dvoretsky, Z. D. Kvon, J. Ziegler, D. Weiss, and S. D. Ganichev, Phys. Rev. B **95**, 201103(R) (2017).

13. S. N. Artemenko and V. O. Kaladzhyan, JETP Lett. **97**, 82 (2013).

14. L. I. Magarill and M. V. Entin, JETP Lett. **104**, 771 (2016).

15. M. L. Savchenko, Z. D. Kvon, S. Candussio, N. N. Mikhailov, S. A. Dvoretskii, and S. D. Ganichev, JETP Lett. **108**, 247 (2018).

16. E. B. Olshanetsky, Z. D. Kvon, N. N. Mikhailov, E. G. Novik, I. O. Parm, and S. A. Dvoretsky, Solid State Commun. **152**, 265 (2012).

17. S. Das Sarma, M. P. Lilly, E. H. Hwang, L. N. Pfeifer, K. W. West, and J. L. Reno, Phys. Rev. Lett. **94**, 136401 (2005).

18. T. Ando, A. Fowler, and F. Stern, Rev. Mod. Phys. **54**, 437 (1982).

19. A. D. Chepelianskii and D. L. Shepelyansky, Phys. Rev. B **97**, 125415 (2018).

20. A. A. Zaboltnykh and V. A. Volkov, Phys. Rev. B **99**, 165304 (2019).

21. G. M. Gusev, O. E. Raichev, E. B. Olshanetsky, A. D. Levin, Z. D. Kvon, N. N. Mikhailov, and S. A. Dvoretsky, 2D Mater. **6**, 014001 (2018).

22. G. M. Gusev, E. B. Olshanetsky, Z. D. Kvon, L. I. Magarill, M. V. Entin, A. Levin, and N. N. Mikhailov, JETP Lett. **107**, 789 (2018).

23. O. E. Parfenov and F. A. Shklyaruk, Semiconductors **41**, 1021 (2007).

24. J. Ziman, *Principles of the Theory of Solids* (Cambridge Univ., Cambridge, 1976).

25. N. V. Zavaritskii and Z. D. Kvon, JETP Lett. **38**, 97 (1983).

Translated by R. Tyapaev